




# An Observational Revisit of Stationary Type IV Solar Radio Bursts

Maoshui Lv<sup>1,2</sup> · Yao Chen<sup>1,2</sup>  · V. Vasanth<sup>3</sup> ·  
Mohd Shazwan Radzi<sup>4</sup> · Zamri Zainal Abidin<sup>4</sup> ·  
Christian Monstein<sup>5</sup>

Received: 6 August 2020 / Accepted: 11 January 2021 / Published online: 15 February 2021  
© The Author(s), under exclusive licence to Springer Nature B.V. part of Springer Nature 2021

**Abstract** Stationary type IV solar radio bursts (IVSs) are broadband continuum emission observed at decimetric–decametric wavelength without apparent source motions. They are closely associated with solar flares and/or coronal mass ejections. Earlier studies on IVSs suffered from limited number of events, frequency coverage and available channels, and spatial resolution. Here we present an analysis on 34 IVSs using two-dimensional imaging data provided by Nançay Radioheliograph (NRH) at 10 frequencies from 150 to 445 MHz. The events are recorded from 2010 to 2014. We focus on general properties including the spatial dispersion of sources with frequency, brightness temperature ( $T_B$ ) and corresponding spectra, and polarization. Main findings are: (i) In the majority of events (23/34) regular and systematic source dispersion with frequency can be clearly recognized. (ii) In most (31/34) events the maximum brightness temperature ( $T_{BM}^E$ ) exceeds  $10^8$  K, and exceeds  $10^9$  K in 23 events. The histogram distribution of  $T_{BM}^f$ , i.e. the maximum brightness temperature of a source at certain frequency ( $f$ ) of a specific event (referred to as event- $f$  source, there are 247 such sources in total) exhibits a clear declining trend with increasing frequencies. The dominant type of  $T_B$  spectra is power-law like with a negative index. (iii) In most events (30/34) the sense of polarization remains unchanged and the number of events with right and left-handed polarization are comparable. In 57% of all 247 event- $f$  sources the level of

**Supplementary Information** The online version contains supplementary material available at <https://doi.org/10.1007/s11207-021-01769-6>.

✉ Y. Chen  
[yaochen@sdu.edu.cn](mailto:yaochen@sdu.edu.cn)

M. Lv  
[lvmaoshui@sdu.edu.cn](mailto:lvmaoshui@sdu.edu.cn)

<sup>1</sup> Institute of Space Sciences, Shandong University, Shandong, China

<sup>2</sup> Institute of Frontier and Interdisciplinary Science, Shandong University, Shandong, China

<sup>3</sup> Department of Science and Humanities, Sree Sowdambika College of Engineering, Aruppukottai, India

<sup>4</sup> Radio Cosmology Lab, Physics Department, Faculty of Science, University of Malaya, 50603 Kuala Lumpur, Malaysia

<sup>5</sup> Istituto Ricerche Solari Locarno (IRSOL), Via Patocchi 57, 6605 Locarno Monti, Switzerland

polarization does not change considerably, in about 39% sources the level of polarization exhibits significant variation yet with a fixed sense, and in only 4% the sense of polarization changes. These results provide strong constraints on radiation mechanism of IVSs.

**Keywords** Corona, radio emission · Radio bursts, Type IV

## 1. Introduction

Type IV solar radio bursts represent broadband continuum emission from the solar atmosphere at decimetric–decametric wavelength, first classified by Boischoat and Denisse (1957), while the flare continuum represents their counterpart extending to higher frequency. The two continuum bursts are not separable as seen from the dynamic spectra of some events. Therefore, it has been suggested that the two bursts are released by the same radiation mechanism (e.g. Robinson, 1978; Winglee and Dulk, 1986). Two subgroups have been further defined, including moving (IVM) and stationary (IVS) bursts (Weiss, 1963). For IVMs the spectra show an overall drift from high to low frequencies with sources propagating outward gradually according to available radioheliograph or interferometric data, while for IVSs the spectra show no overall drift and the sources remain stationary (Weiss, 1963; Dulk, 1985). The latter group of events is more often observed (Dulk, 1985).

Both subgroups are associated with energetic electrons accelerated during solar eruptions. IVSs are closely related to solar flares and/or coronal mass ejections (CMEs) (e.g. Carley et al., 2017; Salas-Matamoros and Klein, 2020), and IVMs are thought to be originated from a part of the ejecta of coronal mass ejections, such as outward-moving arcades of loops, plasmoids, or flux ropes (e.g. Smerd and Dulk, 1971; Vlahos, Gergely, and Papadopoulos, 1982; Stewart, 1985; Carley et al., 2017). They carry valuable information about the eruptive process, energetic electrons, as well as magnetic and plasma conditions of the corona, thus, observational characteristics of type IV bursts, as well as other types of radio bursts, can be used to reveal these information with a good knowledge of underlying emission mechanism(s) (e.g. Vasanth et al., 2016, 2019; Carley et al., 2017; Morosan et al., 2019). At present, it is quite controversial regarding whether coherent plasma emission or incoherent gyrosynchrotron emission plays a dominant role for both groups of type IV bursts (e.g. Dulk, 1973, 1985; Kai, 1979; Melrose, 1975; Duncan, 1981; Wagner et al., 1981; Gary et al., 1985; Gopalswamy and Kundu, 1989a; Pick et al., 2005).

To determine the exact emission mechanism for each group of type IV bursts, it is critical to gather observational characteristics of radio bursts, such as values of brightness temperature ( $T_B$ ),  $T_B$  or flux-density spectra, level and sense of polarization, and spatial dispersion of sources with frequency. A very high  $T_B$  ( $> 10^9$  K) can be used as a good indicator of coherent emission, besides well-separated and compact sources at different frequencies also point to coherent emission. The latter point indicates that the emitting frequencies sensitively depend on source locations, this is an essential result of classical coherent emission mechanisms of both plasma emission (Ginzburg and Zhelezniakov, 1958) and electron cyclotron maser (ECM) emission (Wu and Lee, 1979). In addition, sense and level of polarization also contain critical information on the nature of the radio wave, i.e. whether it belongs to X-mode or O-mode or their mixture (e.g. Salas-Matamoros and Klein, 2020).

In an earlier study, Weiss (1963) presented an analysis of 24 type IV bursts using both interferometric (40 and 70 MHz) and spectral (15–210 MHz) data. According to the movements of sources at different frequencies, they separated the events into two groups, designated as moving and stationary type IV bursts. They reported no appreciable dispersion of

source position over the narrow range of interferometric frequencies available then. Clavelier, Jarry, and Pick (1968) studied 13 IVSs (or noise storm enhancements) based on interferometric and flux data recorded at two frequencies (169 and 408 MHz). Particular interest was the double-source morphology found in seven events. They reported that the source positions at 169 and 408 MHz do not coincide, and further suggested that the radiation is either plasma emission related to the plasma frequency or gyromagnetic emission of subrelativistic electrons related to the gyrofrequency. Note that these earlier data are interferometric and only for two frequencies with quite limited spatial resolution, thus the results should not be regarded as conclusive.

To further explore observational constraints on emission mechanisms, it is important to use 2D radioheliograph data covering more frequencies. It is also useful to make comparisons between properties of events of the two subgroups of type IV bursts. One earlier study with 2D radioheliograph data was conducted for 44 IVMs observed with Culgoora (Duncan, 1981). They investigated the  $T_B$  distribution, level of polarization, and source dispersion at three frequencies (43, 80, and 160 MHz). Signatures of spatial dispersion with frequency have been reported. From this together with other observations, the author suggested that the radio bursts are not given by gyrosynchrotron, but through Langmuir-wave conversion of plasma emission.

Since 1990s, Nançay Radioheliograph (NRH: Kerdraon and Delouis, 1997) conducts routine observation of metric radio bursts, providing two-dimensional images of solar radio bursts for ten frequency channels from 150 to 445 MHz. This is extremely useful to examine relative spatial location of sources at different frequencies, as well as variation of other properties with frequency and time. In addition, multi-wavelength EUV data from the high-resolution data of the Atmospheric Imaging Assembly (AIA) onboard the Solar Dynamics Observatory (SDO: Pesnell, Thompson, and Chamberlin, 2012) can be used to infer plasma properties such as density and temperature around the radio sources when simultaneous data from both NRH and SDO are available. In recent years, several studies on type IV bursts along this line, including IVMs and IVSs, have been reported (e.g. Tun and Vourlidas, 2013; Bain et al., 2014; Vasanth et al., 2016, 2019; Carley et al., 2017; Liu et al., 2018; Morosan et al., 2019; Salas-Matamoros and Klein, 2020).

Tun and Vourlidas (2013) and Bain et al. (2014) analyzed the IVM event dated on 14 August 2010, combining data from NRH and SDO. They found that the IVM sources present no spatial dispersion with frequency and the source intensity is relatively weak. This leads them to conclude that the burst is given by gyrosynchrotron. In two case studies of IVMs that are observed on 4 March 2012 and 15 June 2014, respectively, Vasanth et al. (2016, 2019) showed that in both events the sources at different frequencies present a regular spatial dispersion with relatively high  $T_B$  ( $10^8 - 10^9$  K). In addition, the sources are found to be closely correlated with the top part of the high-temperature bright ejecta of the associated CME. They concluded that IVMs are coherent emission excited by energetic electrons trapped within the hot eruptive structure (see Li et al., 2019 and Ni et al., 2020 for latest studies on emission mechanism relevant to IVMs).

A latest study on an IVS event dated on 24 September 2011 using both NRH and SDO data by Liu et al. (2018) also revealed an obvious spatial dispersion of sources with lower-frequency sources being further away from the Sun. In addition, they reported a very high  $T_B$  over  $10^{11}$  K at 150 MHz, high polarization levels, and a power-law like spectrum. This leads the authors to suggest that the coherent ECM emission may be relevant.

These case and statistical studies show that emission mechanisms of both IVMs and IVSs remain debatable. This is partly due to observational limitations of earlier and present radio instruments, in particular, the quite limited spatial resolution, frequency coverage and/or

available channels. In this study, we focus on IVS events for simplicity. Characteristics of 34 IVS events observed by NRH from 2010 to 2014 are summarized. The criteria used to build the data sample are introduced in the following section together with observational details of one specific event. Classification schemes of event characteristics, and results of our analysis are presented in Section 3. Summary and discussion are given in the last section.

## 2. Observational Data

In the present study we consider IVSs observed from 2010 to 2014, keeping in mind that the SDO data are also available and future studies may further explore their source properties. The IVSs are selected using dynamic spectral data recorded by the e-Callisto Bleien Radio Observatory (Benz et al., 2009) in the range of 175–500 MHz, and data from other e-Callisto observatories in the range of 100–175 MHz. The selection criteria can be summarized as: (i) the bursts should present a wide-band continuum without an obvious general trend of spectral drift; (ii) the bursts should extend to frequency below 300 MHz, with a bandwidth larger than 100 MHz and a duration of at least five minutes; (iii) the bursts should be observed with NRH. In addition, if the time separation of two bursts is less than 30 minutes, they are identified as one event, otherwise two events will be counted. Decimetric continuum bursts were included as long as the above criteria were satisfied. Sources observed by NRH were carefully checked to make sure that all bursts belong to the stationary type.

NRH provides imaging data at 10 frequencies (150, 173, 228, 270, 298, 327, 360, 408, 432, and 445 MHz). The spatial resolution depends on frequency and time of observation, being  $\approx 2'$  at 445 MHz and  $\approx 6'$  at 150 MHz in summer and up to three times larger for the NS direction during winter. The calibration of NRH is performed with one of the strongest wide-band radio sources in the sky (the radio galaxy Cygnus A; see Kerdraon and Delouis, 1997; Mercier et al., 2015). This is completed with a self-calibration process about every two weeks. The data with 10s cadence are used. In many cases there appear more-than-one sources simultaneously for a given frequency at a certain time. For simplicity, we skip these data and only analyze data with simple single-source morphology at all available frequencies. To lay out the basis for further analysis, we show details of the specific Event 20120304.

In Figure 1, we show NRH images observed at 11:07:07 UT, superposed by four contours at levels of 65, 75, 85, and 95% of the maximum brightness temperature observed at the moment and corresponding frequency ( $T_{\text{BM}}$ ). The images have been CLEANed using the NRH software. The weak features outside of the source with the  $T_{\text{BM}}$  are most likely due to noise and not real sources. Note that data used in further analysis are directly downloaded from NRH website solar radio data base, and not CLEANed to the best of our knowledge. This does not affect our results since we are mainly interested in sources with  $T_{\text{BM}}$ . The values of  $T_{\text{BM}}$  are given in the figure. The lower right panel presents the corresponding dynamic spectrum. The interval of interest has been labeled with two vertical dashed lines and the solid line represents the moment of NRH images shown in the figure. The wide-band-continuum nature of the event is clear, and all  $T_{\text{BM}}$ s are above  $10^9$  K.

In Figure 2a and the online movie (M1), we plot NRH source contours at different frequencies together to examine their relative location. It is clear that different sources show a clear pattern of spatial dispersion. The sources line up regularly in the order of their frequency, with those at higher frequency being closer to the disk. Together they form a morphology of a loop section. The values of  $T_{\text{BM}}$  have been presented in the figure. Note that

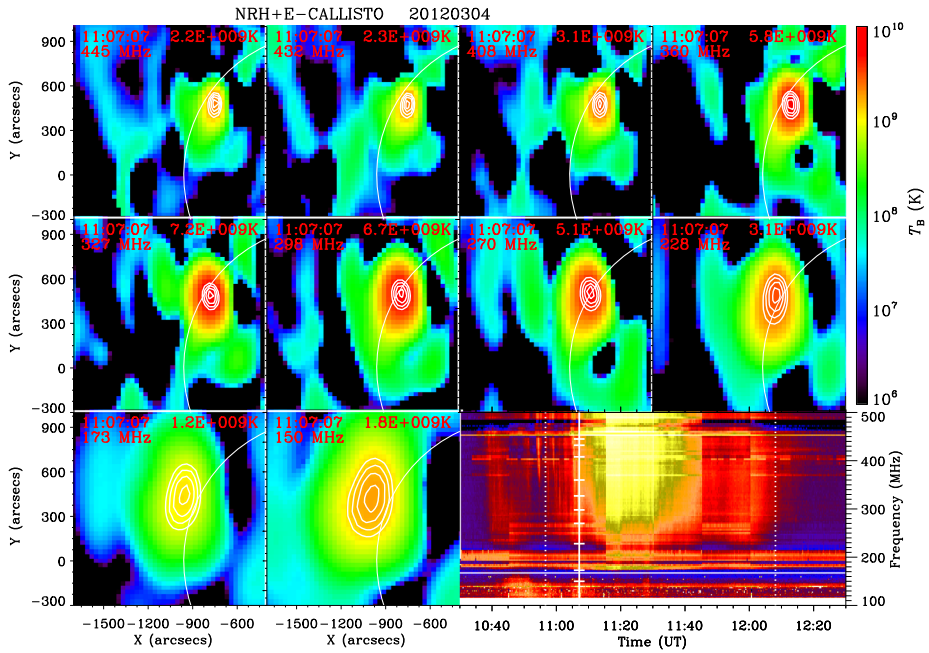


**Figure 1** NRH images at different frequencies and the dynamic spectrum of Event 20120304. The NRH images were processed using the multi-scale CLEAN algorithm included within the standard NRH software. The contours are given by the 65, 75, 85, and 95% levels of the maximum  $T_B$  ( $T_{BM}$ ). Values of  $T_{BM}$  have been presented in the figure. The vertical solid line in the spectrum indicates the moment of radio images and the short horizontal lines represent the corresponding frequencies of NRH. The two vertical dotted lines indicate the interval of interest.

similar formation of NRH sources has been reported by Liu et al. (2018) for a IVS event and by Vasanth et al. (2016, 2019) for two IVM events. In further analysis we classify events into two groups according to whether the source dispersion is obvious or not.

In Figures 2b–c, we plot the temporal profiles of  $T_{BM}$  and the corresponding spectra given by the variation of one-minute averaged  $T_{BM}$ , at two selected moments (10:56:57 and 11:06:57 UT). Values of the maximum  $T_{BM}$  during the whole interval of interest (referred to as  $T_{BM}^f$  hereinafter) have been presented in panel b.

From panel b, it can be seen that  $T_{BM}^f$  varies from  $2.9 \times 10^9$  to  $1.1 \times 10^{10}$  K, and  $T_{BM}$  varies similarly for almost all frequencies with a first-increase-then-decrease trend, except for the two lowest frequencies (150 and 173 MHz) at which the profiles exhibit strong variability. From panel c, it can be seen that at 10:56:57 UT the spectrum shows a first-decrease-then-increase profile with increasing frequencies, while at 11:06:57 UT the spectrum presents a first-increase-then-decrease profile if neglecting the data at the lowest frequency (150 MHz). The total duration of the interval is 71 minutes, therefore we obtain 71 sets of one-minute averaged spectra of  $T_{BM}$ . These spectra present several types of spectral shape. Further classification according to the shape will be presented in Section 3.

In Figure 2d we plot temporal profiles of polarization degree ( $p$ ) at each frequency, with  $p$  given by

$$p = \frac{\sum(I_R - I_L)}{\sum(I_R + I_L)} \tag{1}$$

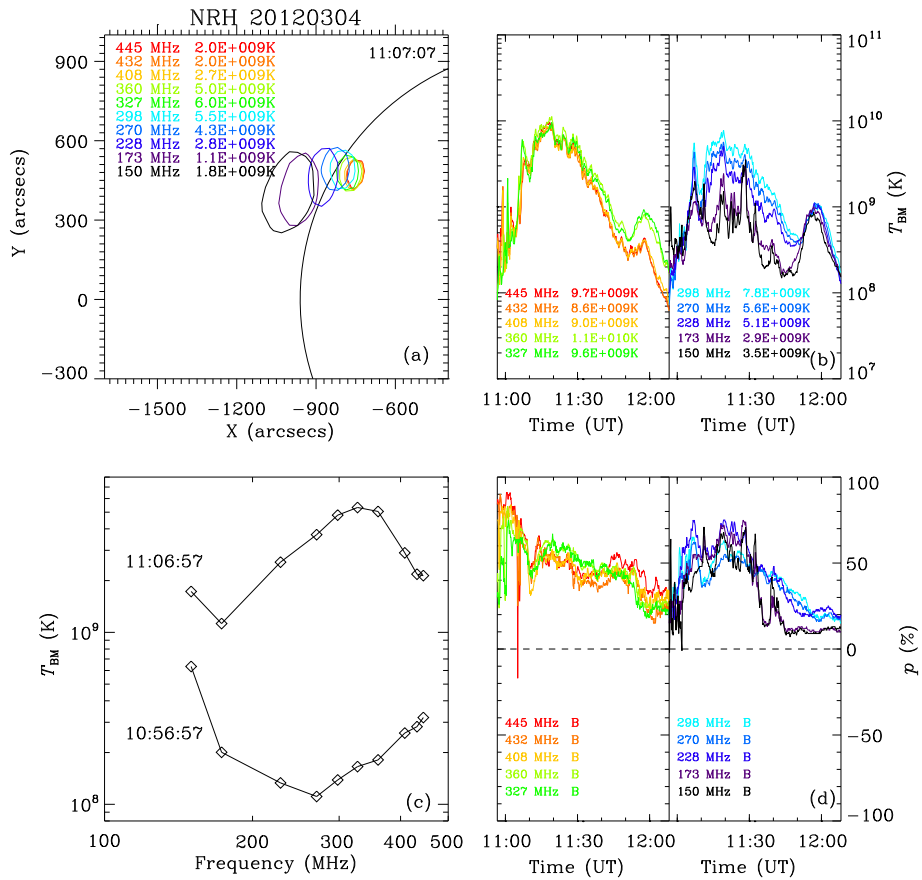


**Figure 2** (a) Contours of NRH sources superposed together, (b) temporal profiles of  $T_{\text{BM}}$ , (c) the corresponding spectra, and (d) temporal profiles of polarization of Event 20120304. The contours in panel a are given by the 85% levels of the  $T_{\text{BM}}$  at all frequencies. The values of  $T_{\text{BM}}$  and their maximum during the interval of interest ( $T_{\text{BM}}^f$ ) have been presented on panels a and b. An animation is available as online supplementary material (M1).

with  $I_{\text{R}}$  and  $I_{\text{L}}$  representing the fluxes of right- and left-handed polarization, respectively, the sum is over the region within the contour at the level of 85% of  $T_{\text{BM}}$ . Note that we have removed data with  $|p|$  larger than 100% for all events investigated here. Such data are unphysical, likely due to problems associated with the procedures of data processing, such as Fourier transform, calibration, or removal of radio interference.

It can be seen that during the interval of interest the sense of polarization remains unchanged while the degree ( $p$ ) changes significantly for all frequencies. For frequencies within 150–298 MHz,  $p$  first increases to a local maximum about 50–80%, and then decreases to a weak level around 10–30%; for most frequencies within 327–445 MHz,  $p$  presents an overall declining trend from a strong level of about 60–90% to a moderate level of about 20–40%. Further analysis will classify events according to  $p$  and its variation.

Major characteristics of the 34 IVSS events are listed in Table 1. The different columns are as follows:

**Table 1** List of IVs and the characteristics of their spatial dispersion,  $T_{BM}^f$ , and polarization. Figures in brackets indicate the numbers of available NRH frequencies. See text presented in Section 2 for detailed explanation of the different columns.

Event	Bleien spectrum		NRH source location	$T_{BM}^f$	Level and sense of polarization	Classification according to polarization
	Start time (UT)	End time (UT)				
20100814 (L, I)	09:40	10:50	N03W57	150 (1): H 173-445 (9): M	150-360 (7) (+); 408-445 (3) (I): W, M	150-360 (7): B 408-445 (3): C
20110307 (D, I)	14:16	14:45	N28E21	150-173 (2): H 228-360 (5): M	150-173 (2) (-); 298 (1) (I): W, M 228-270, 327-360 (4) (I): W, M, S	150-173 (2): B 228-360 (5): C
20110809 (L, I)	08:31	08:56	N05W72	150-445 (10): M	150-173 (2) (+): M 228-327, 408, 445 (6) (+) 360, 432 (2): W	150-173 (2): B 228-445 (8): A
20110924 (L, I)	12:32	14:23	N05E55	150-360, 432-445 (9): H	150-445 (9) (-): S	150-173 (2): B 228-445 (7): A
20110925 (L, II)	09:40	10:40	PA 243	298-445 (6): M	298-445 (6) (+): M	298-445 (6): A
20111005 (L, I)	11:14	11:24	PA 110	298-445 (6): M	298-360 (3) (-): W 408-432 (2) (-); 445 (1) (I): W, M	298-360 (3): A 408-432 (2): B 445 (1): C
20120304 (L, I)	10:35	12:15	N26E64	150, 228-445 (9): H 173 (1): M	150-327 (6) (+): W, M 360-445 (4) (+): W, M, S	150-445 (10): B
20120305 (L, I)	08:50	09:03	N26E53	150-445 (10): M	150-445 (10) (+): S	150-445 (10): A
20120314 (D, I)	15:17	15:26	N19E03	150-360 (7): M 408-445 (3): L	150-327, 408, 445 (8); 360, 432 (2) (-): W	150-445 (10): A
20120418 (D, I)	12:51	13:40	S21W41	150-445 (9): M	150-228 (3) (+): M, S 270-445 (6) (+): S	150-228 (3): B 270-445 (6): A
20120507 (L, I)	14:36	14:41	S17W58	150-327 (6): M 408-445 (3): L	150-173 (2) (+): W, M 228 (1) (+): M 270-327 (3) (+); 408-445 (3): W	150-173 (2): B 228-445 (7): A

**Table 1** (Continued)

Event	Bleien spectrum		Duration (Mins)	NRH source location	$T_{\text{BM}}^f$	Level and sense of polarization	Classification according to polarization
	Start time (UT)	End time (UT)					
20120530 (L, I)	09:43	10:00	17	PA 104	298, 408-445 (4): L 327 (1): M	298-445 (5): W	298-445 (5): A
20120613 (D, I)	12:55	14:30	95	S33E12	150 (1): H 173-327 (5): M	150-173 (2) (+): W 228 (1) (+): W, M 270-327 (3) (+): W, M, S 150-327 (6) (-): W, M, S	150-327(6): B 150-327 (6): B
20120614 (D, I)	13:24	15:10	106	S21E10	150-228 (3): H 270-327 (3): M		150-327 (6): B
20120630 (D, I)	08:26	08:44	18	S12E25	228-432 (6): M 445 (1): L	228-327 (4); 408-445 (3) (-): W	228-445 (7): A
20120708 (L, I)	10:23	10:30	7	PA 250	228-445 (7): L	228-298, 408-445 (6) (-); 327 (1): W	228-445 (7): A
20120710 (D, II)	08:37	08:45	8	S19E14	150, 327-445 (5): M 173-298 (4): L	150-445 (9): W	150-445 (9): A
20121214 (D, II)	08:48	09:03	15	N09W22	150-445 (9): L	150-173, 270-327 (5) (-): M 228, 408-445 (4) (-): M, S 150-445 (8) (-): S	150-173, 270-327 (5): A 228, 408-445 (4): B 150-445 (8): A
20130411 (D, II)	08:27	08:32	5	N12E10	150-173 (2): H 270-445 (6): M		
20130517 (L, II)	08:51	09:07	16	N17E52	270-445 (6): M	270-327 (3) (-): W	270-327 (3): A
20130520 (D, I)	11:02	11:37	35	N23W16	270-445 (6): M	408-445 (3) (-): W, M 270-445 (6) (+): W	408-445 (3): B 270-445 (6): B
20130522 (L, II)	13:10	13:17	7	N17W85	298-445 (4): L	298 (1) (+): M 408-445 (3) (+): W, M 150-432 (8): W	298 (1): A 408-445 (3): B 150-432 (8): A
20130605 (L, I)	08:41	09:03	22	PA 243	150-327 (6): M 408-432 (2): L		
20130812 (D, I)	11:04	11:36	32	S24E20	150-298 (5): M 327 (1): L	150-173 (2) (+): W 228-298 (3) (+): W, M 327 (1) (+): M	150-173 (2): A 228-327 (4): B



**Table 1** (Continued)

Event	Bleien spectrum		Duration (Mins)	NRH source location	$T_{BM}^f$	Level and sense of polarization	Classification according to polarization
	Start time (UT)	End time (UT)					
20131025-1 (L, II)	08:58	09:08	10	PA 106	173-327 (5): M	173, 327 (2) (+): W, M 228-298 (3) (+): M	173-270, 327 (4): B 298 (1): A
20131025-2 (L, I)	14:59	15:10	11	S18E77	298-445 (4): M	298-327, 432 (3) (+): W, M 408 (1) (+): W	298-445 (4): B
20131026 (L, II)	11:12	11:42	30	S16E64	270-298 (2): M 327-445 (3): H	270-327 (3) (+): W, M 408-445 (2) (+): W, M, S	270-445 (5): B
20131107 (D, I)	14:30	15:10	40	S43E32	173-327 (5): M 408-445 (2): L	173-228 (2) (+): 298 (1) (-): W, M 270 (1) (I): W 327-445 (3) (-): W, M, S	173-228, 298-445 (6): B 270 (1): C
20131119 (L, I)	11:07	11:38	31	PA 257	150-173, 408, 445 (4): H 228-327 (4): M	150-327, 445 (7): 408 (1) (-): W	150-445 (8): A
20131223 (D, I)	12:43	12:59	16	S17E12	150-228 (3): H 270-327 (3): M 408-432 (2): L	150-432 (8) (+): S	150-432 (8): A
20140211-1 (D, I)	10:48	10:55	7	S08E15	150-432 (8): M	150-327 (6) (-): M 408-432 (2) (-): S	150-432 (8): B
20140211-2 (D, II)	14:35	14:42	7	S08E06	150, 270-327 (3): M 173 (1): H 408-432 (2): L	150 (1) (-): S 173-327 (3) (-): M 408-432 (2) (-): M, S	150-270 (3): A 327-432 (3): B
20140216 (D, II)	09:23	09:38	15	S10W05	150-432 (8): H	150-173 (2) (+): W, M, S 228-298 (3) (+): M, S 327-432 (3) (+): S	150-298 (5): B 327-432 (3): A
20140821 (D, II)	11:56	12:07	11	S04E42	270-327 (3): M 408-445 (2): L	270-445 (5) (+): S	270-445 (5): A

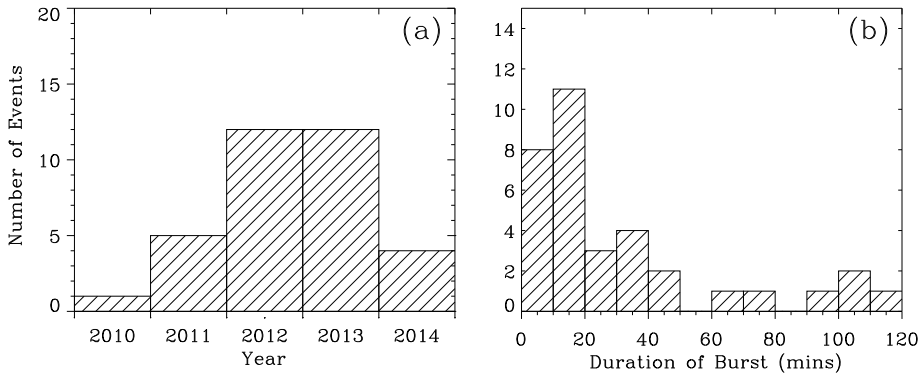
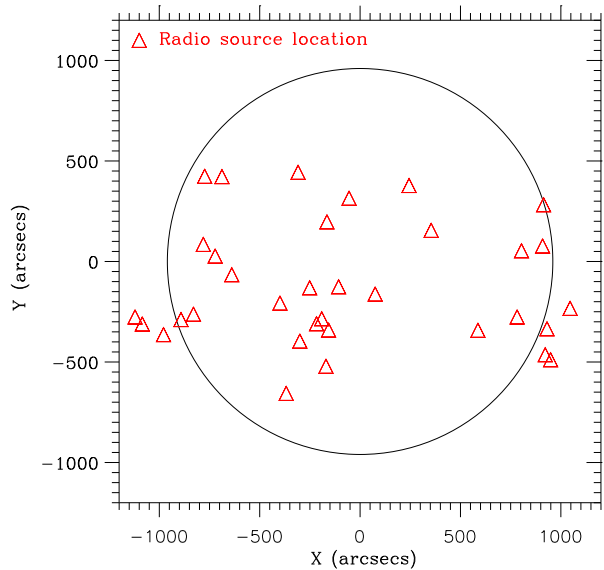


**Figure 3** Histograms of occurrence times (a) and durations (b) of the 34 IVSs.

- (i) In column one, we present dates of events, whether it is a limb (L) or disk (D) event, and its group according to the characteristics of the source spatial dispersion at different frequencies, with group I for events with clear systematic source dispersion and group II for those without clear systematic dispersion. In Section 3.1 more details will be presented to show how we classify events into these two groups.
- (ii) In columns two–four, we present the start and end time, and duration of the IVS spectrum according to the dynamic spectral data.
- (iii) In column five, we present the source location at the highest frequency available for each event. The source location is represented by the source centroid which corresponds to the location of  $T_{\text{BM}}^f$ . Averaged location of the centroid has been used during the interval of interest. For sources outside the limb, position angle (PA) of the averaged location of source centroid has been used. The PA is set to be 0 along the northward direction and increases counterclockwise.
- (iv) In column six, we present classifications of sources according to the magnitude of  $T_{\text{BM}}^f$ , with H being high ( $T_{\text{BM}}^f \geq 10^{9.5}$  K), M being moderate ( $10^8 \text{ K} \leq T_{\text{BM}}^f < 10^{9.5}$  K), and L being low ( $T_{\text{BM}}^f < 10^8$  K). The figure in brackets indicates the number of frequency channels available in NRH data. This also applies to numbers in brackets in columns seven and eight.
- (v) In column seven, we present level and sense of polarization at each frequency and event. ‘+’ means  $p > 0$  and ‘-’ means  $p < 0$  and ‘I’ means sign of  $p$  changes significantly, i.e. with inversion(s) of sense, during the interval of interest. Numbers between parentheses represent available numbers of NRH frequencies. According to the value of  $p$ , we have classified the sources into three groups, W for weak level ( $|p| < \approx 30\%$ ), M for moderate level ( $\approx 30\% < |p| < \approx 70\%$ ), and S for strong level ( $|p| > \approx 70\%$ ) of polarization.
- (vi) In column eight, we present the classification of sources according to their temporal variation of  $p$  during the interval of interest, with A for sources whose  $p$  does not vary significantly and manifests a fixed sense, and B for sources whose  $p$  varies significantly yet the sense still remains fixed, and C for sources with inversion(s) of polarization sense.

In Figures 3a–b, we present histograms of the occurrence times and durations of all IVSs events. It can be seen that most events occur in 2012 (12/34) and 2013 (12/34), and only five (four) events in 2011 (2014). Due to the limited number of events of the database, we do

**Figure 4** Distribution of source locations of the 34 IVSs. The source location is represented by the averaged source centroid (corresponding to  $T_{BM}$ ) at the highest available frequency during the interval of interest. The black circle represents the solar limb.



not analyze solar cycle dependence of event occurrence. The durations distribute within a large range, from a few to 120 minutes, with more than half (19/34) events lasting for less than 20 minutes, and a few (6/34) lasting for more than 60 minutes. In Figure 4, we present the distribution of source locations. Note that exact locations have been given in Table 1 by the averaged source centroid (corresponding to  $T_{BM}$ ) at the highest available frequency during the interval of interest. We see that all disk sources are located in middle-low latitude (N28–S43), and PAs of seven sources outside the solar disk distribute within two narrow ranges, with three sources within 100–110°, and four within 240–260°; see Table 1 for exact values of PA. Among the seven events, five belong to group I with clear systematic spatial dispersion with frequency, and two belong to group II without clear systematic source dispersion.

### 3. Event Classifications and Analysis

In this section, we present the summary of the characteristics of IVS events, including the source location, spatial dispersion of sources with frequency, brightness temperature and shape of relevant spectra, and sense and level of source polarization. In each part, we first classify events according to relevant characteristics, then present numbers and relative proportions of different groups of events. To make the text easy to follow, terminologies of classification used in the study are summarized in Table 2.

#### 3.1. Classification and Analysis According to Source Location

We first classify all events into two groups according to their locations at the highest available frequency, either on the disk (D) or limb (L). Events outside the limb have been classified into the L group. From column one of Table 1, it can be seen that among the 34 events there are equal number (17) of limb and disk events. See Figure 4 for the location of each event.

**Table 2** Summary of terminology.

Location	L	Limb event
	D	Disk event
	I	Sources of clear systematic spatial dispersion with frequency
	II	Sources without clear systematic dispersion with frequency
Brightness temperature ( $T_B$ )	H	High $T_B$ ( $T_{BM}^f \geq 10^{9.5}$ K)
	M	Moderate $T_B$ ( $10^8$ K $\leq T_{BM}^f < 10^{9.5}$ K)
	L	Low $T_B$ ( $T_{BM}^f < 10^8$ K)
Type of $T_B$ spectra	In	$T_{BM}^f$ increases with frequency
	De	$T_{BM}^f$ decreases with frequency
	ID	$T_{BM}^f$ first increases then declines with frequency
	DI	$T_{BM}^f$ first decreases then increases with frequency
	V	Other type of $T_B$ spectra
Level of polarization	S	Strong polarization ( $ p  > \approx 70\%$ )
	M	Moderate polarization ( $\approx 30\% <  p  < \approx 70\%$ )
	W	Weak polarization ( $ p  < \approx 30\%$ )
Sense of polarization	R/+	Right-handed sense ( $p > 0$ )
	L/-	Left-handed sense ( $p < 0$ )
	W	Weak or no discernible sense
	I	With inversion of sense (s)
Temporal variation of polarization	A	No significant variation and a fixed sense
	B	With significant variation and a fixed sense
	C	With inversion of sense (s)

In addition, as done in Figure 2a, for each event we have superposed the 85% contour of  $T_{BM}$  at all available frequencies together to examine their relative location. As demonstrated above, this allows us to tell whether sources at different frequencies exhibit any systematic dispersion. According to this, we separate the events into two groups, of which six typical events are shown in Figure 5. These are:

- (I) Group I includes events that look like the one presented in the previous section, i.e. events with clear systematic spatial dispersion of sources with frequency. See Figures 5a–b for two limb events (Events 20100814 and 20120304), and Figures 5c–d for two disk events (Events 20131223 and 20140211-1). In these events, the sources line up to give a regular formation according to their frequencies, similar to a section of a loop in morphology, as mentioned above. For the two limb events, sources at higher frequencies are closer to the disk. For the two disk events, this conclusion cannot be drawn due to projection effect. In addition, the size of the source exhibits a clear increasing trend with increasing frequencies, observed for most events. Note that the spatial resolution of NRH data is higher for higher frequency. This contributes to the observed size variation with frequency.
- (II) Group II includes events that display no clear systematic pattern of sources lining-up together in order of frequency. The separation of these events from group I is done mainly through visual inspection. We did measure the distance between source cen-

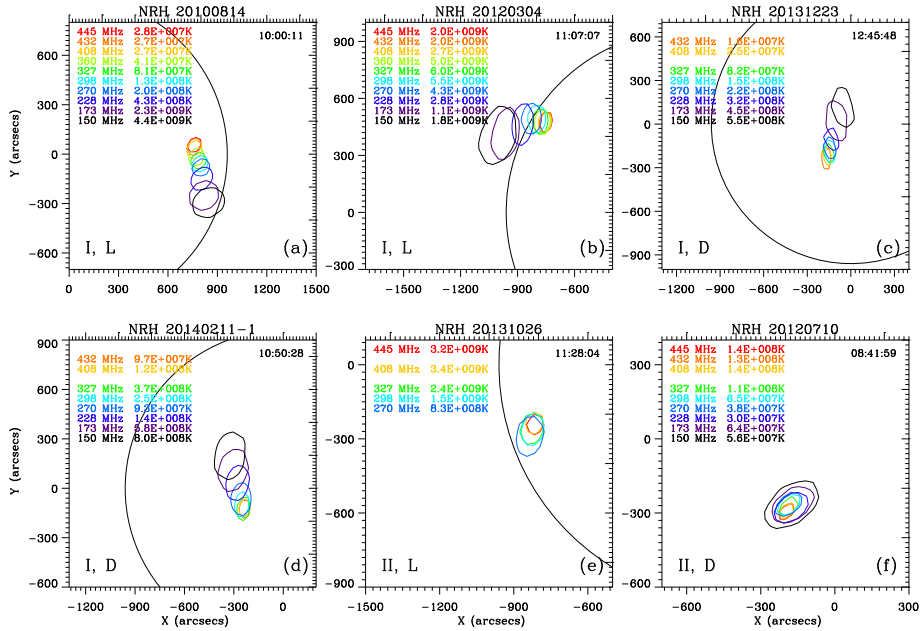


**Figure 5** NRH images of typical events with different types of spatial dispersion. The contours are given by the 85% levels of the  $T_{BM}$  at available frequencies. See text presented in Section 2, relevant to column one in Table 1.

troids at available frequencies of each event, and found that the length of the curved line connecting all centroids being  $\approx 200''$  can be used as a good indicator to separate most events of the two groups. In Figures 5e–f two events of group II are shown with one limb (Event 20131026) and one disk (Event 20120710) event. As stated, no systematic pattern of source dispersion can be identified. This may be partially attributed to projection effect, or the source spatial dispersion is indeed weak. In addition, limited frequency coverage in group II events ( $< 200$  MHz in six of 11 events) also contributes to the absence of dispersion.

Among the 34 events, 23 (68%) can be classified into group I, this means a majority of the events exhibit a pattern of clear systematic spatial dispersion, and 11 (32%) without clear systematic dispersion. The numbers of limb events in group I and group II are comparable to those of disk events. In group I there exist 12 (11) limb (disk) events, and in group II there exist five (six) limb (disk) events. This result has significant implication on candidate emission mechanism of IVSs. Further discussion will be presented in the last section.

### 3.2. Classification and Analysis According to the Brightness Temperatures of Sources

According to values of the maximum brightness temperature ( $T_{BM}^f$ ) for sources at each frequency during a specific event (referred to as event- $f$  sources), we can separate all sources into three groups, including the high  $T_{BM}^f$  (H) group with  $T_{BM}^f \geq 10^{9.5}$  K, the moderate  $T_{BM}^f$  (M) group with  $10^8 \text{ K} \leq T_{BM}^f < 10^{9.5}$  K, and the low  $T_{BM}^f$  (L) group with  $T_{BM}^f < 10^8$  K. In Table 1 we have listed the result of the classification for all available event- $f$  sources.

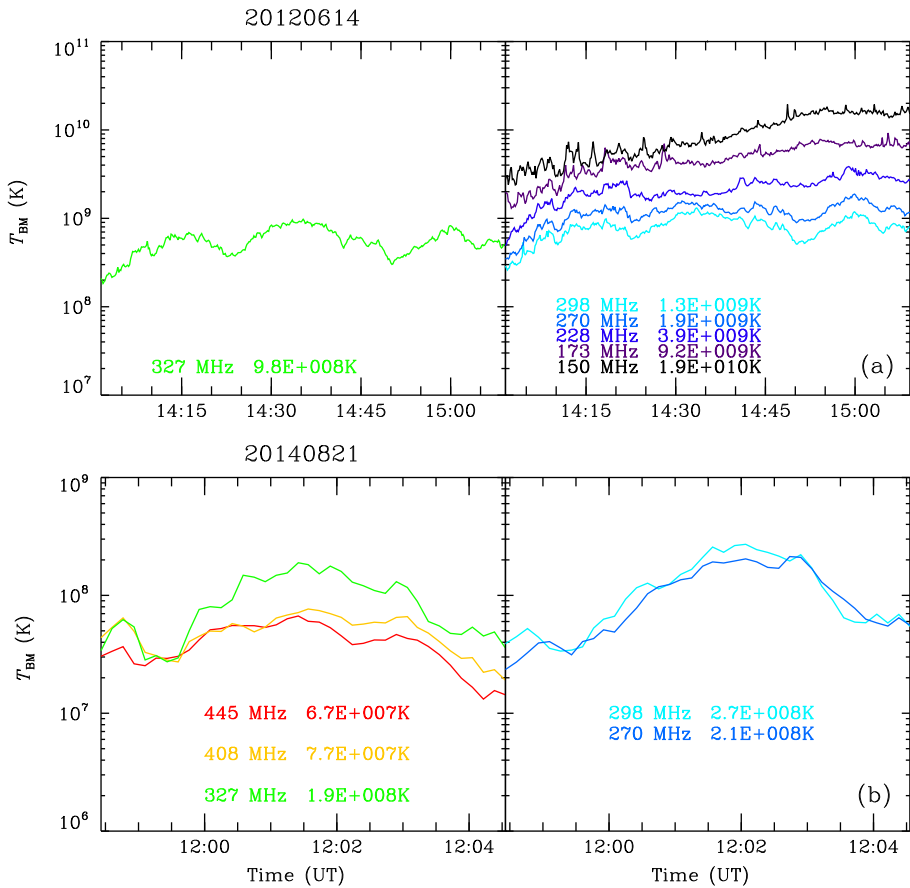


**Figure 6** Typical profiles of  $T_{BM}$  for two events. The values  $T_{BM}^f$  are shown on each panel.

In Figure 6, we present profiles of  $T_{BM}$  for two events. The values of  $T_{BM}^f$  are written on the figure. For Event 20120614 (panel a),  $T_{BM}$  at all frequencies present an oscillatory behavior with an overall increasing trend. The sources at 150–228 MHz belong to the H group with  $T_{BM} \geq 10^{9.5}$  K, and sources at 270–327 MHz belong to the M group. For Event 20140821, similar to the one shown in Figure 2b,  $T_{BM}$  at all frequencies behave similarly with a first-increase-then-decrease trend with a local maximum ( $T_{BM}^f$ ). The sources at 270–327 MHz belong to the M group, and those at 408 and 445 MHz belong to the L group, according to our classification scheme.

In Figure 7a we plot the histogram of  $T_{BM}^f$ s for all the 247 event- $f$  sources. It can be seen that  $T_{BM}^f$ s for all sources display a single-peak distribution, with the peak lying in the interval of  $10^8 \text{ K} \leq T_{BM}^f < 10^{8.5} \text{ K}$ , where 64 (26%) sources are recorded. In the range of  $10^8 \text{ K} \leq T_{BM}^f < 10^{9.5} \text{ K}$ , i.e. the M group, we observe 155 (63%) sources in total. This means that more than half of all sources belong to this group, while sources of the H group are 46 (19%) in number (percentage), being equal to the number (percentage) of sources of the L group.

In Figures 7b–e, we plot histograms of  $T_{BM}^f$  for different groups of sources: panel b for events on the limb (L), panel c for events on the disk (D), panel d for events with clear

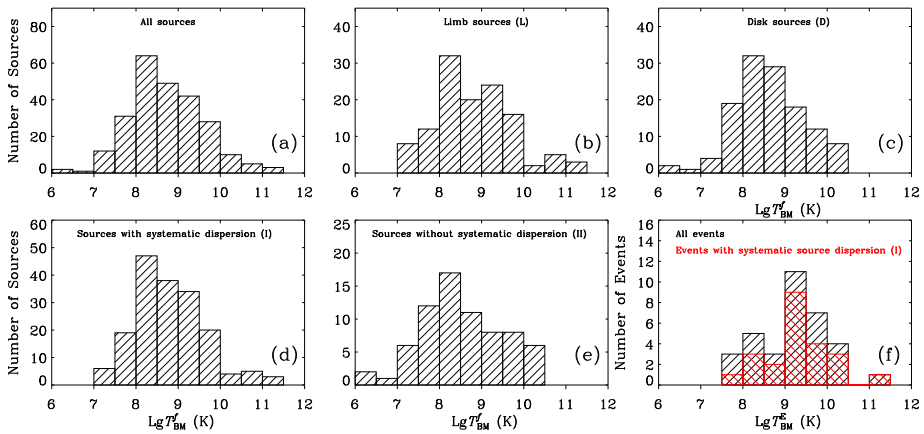


**Figure 7** (a) Histograms of  $T_{\text{BM}}^f$  for all event- $f$  sources, (b) for L-group sources, (c) D-group sources, (d) group I sources, and (e) group II sources. (f) Histogram of the maximum  $T_{\text{B}}$  ( $T_{\text{BM}}^E$ ) for the 34 events, red blocks correspond to group I events.

systematic spatial dispersion of sources (group I), and panel e for events without clear systematic source dispersion (group II). As seen from panel b 76/122 (62%) sources in limb events belong to the M group ( $10^8 \text{ K} \leq T_{\text{BM}}^f < 10^{9.5} \text{ K}$ ). In addition, 79/125 (63%) sources in disk events (panel c), 119/176 (68%) sources of group I events (panel d), and 36/71 (51%) for group II events (panel e) belong to the M group. This means that sources of the M group always represent the largest contribution, in comparison to those of the L and H groups.

For each event, we can obtain a maximum brightness temperature among all available sources ( $T_{\text{BM}}^E$ ). This represents the highest  $T_{\text{B}}$  of one specific event. In total, we get 34 values of  $T_{\text{BM}}^E$ . In the last panel of Figure 7, we show the histogram of these values (black). The distribution of group I (red, with clear systematic spatial dispersion of sources) is also presented. There are 31 (91%) events whose  $T_{\text{BM}}^E$  exceed  $10^8 \text{ K}$ , 23 (68%) events whose  $T_{\text{BM}}^E$  exceed  $10^9 \text{ K}$ , and only three events whose  $T_{\text{BM}}^E$  are lower than  $10^8 \text{ K}$ . There are 11 events whose  $T_{\text{BM}}^E$  are in the range of  $10^9 - 10^{9.5} \text{ K}$  and seven events in the range of  $10^{9.5} - 10^{10} \text{ K}$ . In total, about half of all events (18/34) lie in these two intervals. In addition, group I events seem to provide more high- $T_{\text{BM}}^E$  events, in particular, nine events of this group are in the range of  $10^9 - 10^{9.5} \text{ K}$  and 17 events with  $T_{\text{BM}}^E$  exceeding  $10^9 \text{ K}$ ; accordingly, in group II, only two events whose  $T_{\text{BM}}^E$ s lie in the range of  $10^9 - 10^{9.5} \text{ K}$  and six events whose  $T_{\text{BM}}^E$ s exceed  $10^9 \text{ K}$ .

In Figure 8, we plot histograms of  $T_{\text{BM}}^f$  for all event- $f$  sources at available frequencies, except 360 MHz since only nine events were observed by NRH. Two major characteristics can be listed: (i) distributions of  $T_{\text{BM}}^f$  always manifest one major peak, (ii) values of  $T_{\text{BM}}^f$  at the peaks present a declining trend with increasing frequencies, e.g.  $T_{\text{BM}}^f$  decreases from  $10^{9.5} - 10^{10} \text{ K}$  at 150 MHz to  $10^{7.5} - 10^{8.5} \text{ K}$  at 445 MHz.

### 3.3. Classification and Analysis According to the Spectra of the Brightness Temperature

At any given time, we can plot the spectrum given by the variation of the maximum brightness temperature ( $T_{\text{BM}}$ ) with frequency. All spectra are classified into 5 types according to their profiles. Typical spectra have been presented in Figure 9. They are: (i) spectra with

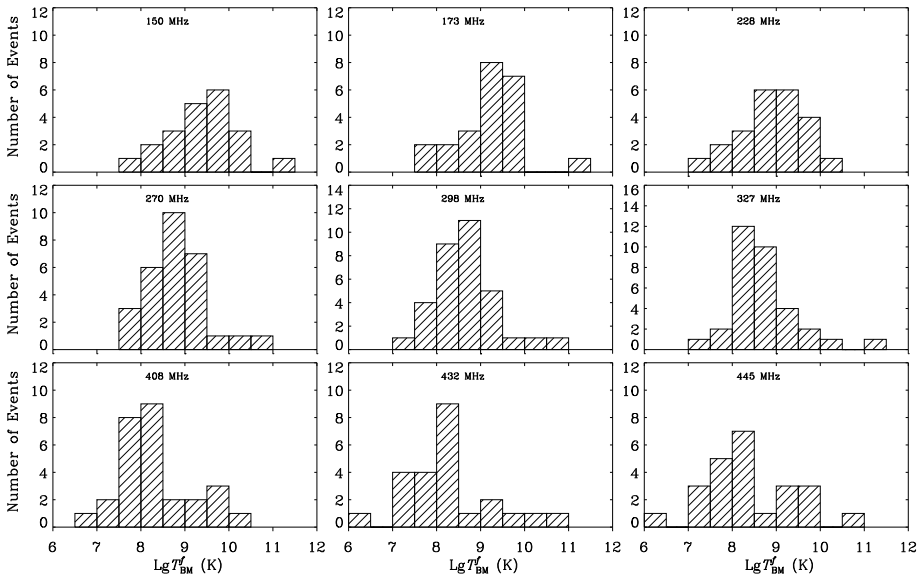


**Figure 8** Histograms of  $T_{BM}^f$  for all event- $f$  sources at available NRH frequencies, except 360 MHz.

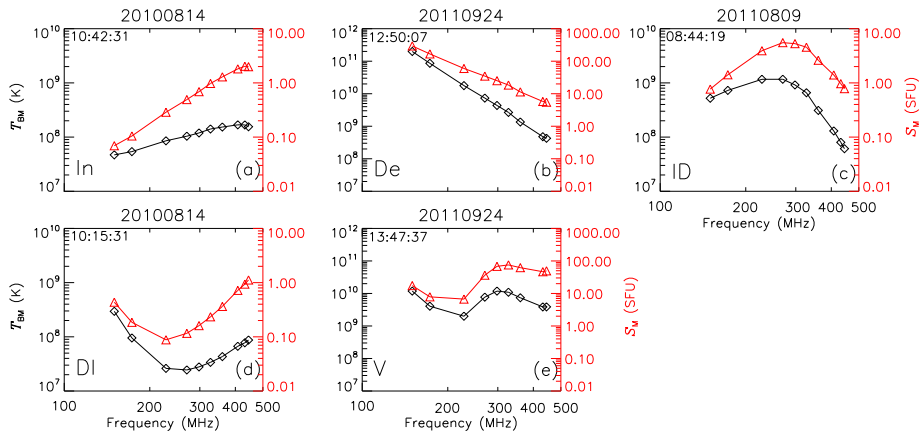


**Figure 9** Typical types of  $T_B$  spectra with the corresponding flux-density spectra. See text in Section 2.

$T_{BM}^f$  increasing in general with frequency, referred to as In-type for short, see Figure 9a for an example; (ii) spectra with  $T_{BM}^f$  decreasing in general with frequency, referred to as De-type, see Figure 9b; (iii) spectra with  $T_{BM}^f$  first-increasing-then-declining with frequency with a well-defined maximum, referred to as ID-type, see Figure 9c; (iv) spectra with  $T_{BM}^f$  first-declining-then-increasing, referred to as DI-type, see Figure 9d; (v) other spectra that cannot be classified into any of the above four groups, mostly with strong variability, referred to as V-type for short, see Figure 9e. The corresponding spectra of flux density are also presented for comparison. The flux-density spectra are also given by the variation of one-minute averaged maximum flux density ( $S_M$ ). It can be seen that the two types of spec-



**Table 3** Numbers/percentages of  $T_B$  spectra in groups classified according to their profiles. See text in Section 2.

Event	In	De	ID	DI	V	Total
20100814 (L, I)	5/9%	16/30%	6/11%	26/48%	1/2%	54
20110307 (D, I)		5/100%				5
20110809 (L, I)			19/100%			19
20110924 (L, I)		47/50%		23/24%	24/26%	94
20120304 (L, I)		1/1%	55/77%	5/7%	10/14%	71
20120305 (L, I)		11/100%				11
20120314 (D, I)		1/20%	4/80%			5
20120418 (D, I)		40/100%				40
20120507 (L, I)		1/33%			2/67%	3
20120613 (D, I)		19/76%	6/24%			67
20120630 (D, I)			1/100%			1
20120708 (L, I)		3/100%				3
20120710 (D, II)				6/100%		6
20121214 (D, II)		14/100%				14
20130411 (D, II)		3/100%				3
20130605 (L, I)		8/44%	9/50%	1/6%		18
20130812 (D, I)		26/100%				26
20131025-1 (L, II)			7/100%			7
20131107 (D, I)		26/100%				26
20131119 (L, I)	2/6%	18/58%		11/35%		31
20131223 (D, I)		7/44%	9/56%			16
20140211-1 (D, I)		5/100%				5
20140211-2 (D, II)		4/80%	1/20%			5
20140216 (D, II)		1/8%	6/50%	1/8%	4/33%	12

tra exhibit similar profiles which are readily transferred from each other via the well-known  $T_B$ - $S$  relation (see, e.g., Dulk, 1985).

As stated, the spectra are given by the one-minute averaged  $T_{BM}$  data. Therefore, the number of spectra for one specific event is determined by the total duration of the event. Since the spectra evolve with time, one event can yield a few to several types of spectra. We have classified all spectral data for 25 events including 19 group I and 6 group II events, and presented the results in Table 3. Note that the other nine events lack NRH data at frequencies below 270 MHz and therefore are not analyzed here.

From this table, it can be seen that 21 events contain the De-type spectra, in 14 events this type of spectra is present in  $\geq 50\%$  of the event duration, and in ten events only this type of spectra is present. In addition, 11 events contain the ID-type spectra, and in eight events this type of spectra is present in  $\geq 50\%$  of the event duration, and in three events only this type of spectra is present. In seven events the DI-type spectra are present, and in only one event the DI-type spectra are present in  $\geq 50\%$  (100%) of the event duration. At last, numbers of events with In- and V-type spectra are two and five, respectively. These results indicate that the dominant type of spectra are the De type, i.e. the power-law like spectra with a negative index, the less important spectra are the ID and DI types, while In- and V-type spectra are the minority.

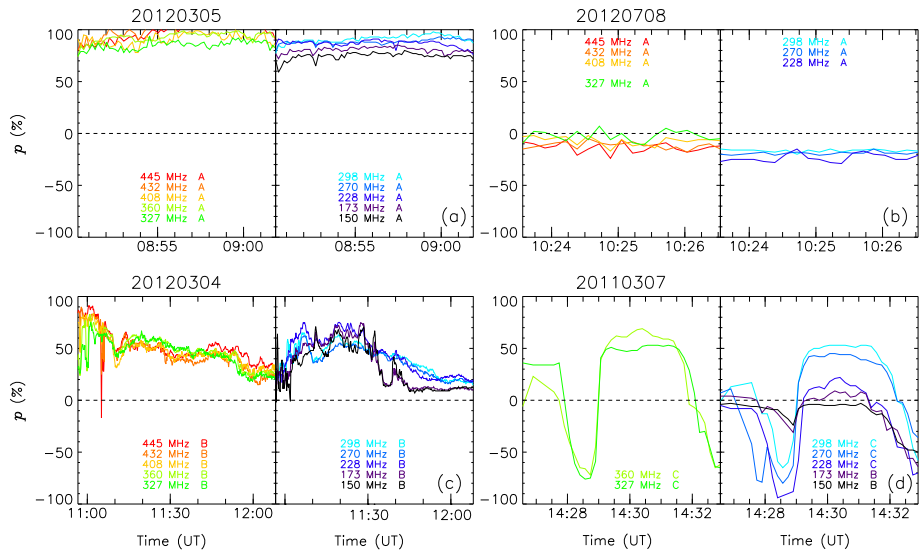


**Figure 10** Typical polarization profiles of four events. See text in Section 2, relevant to column eight in Table 1.

### 3.4. Classification and Analysis According to the Level and Sense of Polarization

All the 247 event- $f$  sources can also be classified according to the level and sense of the polarization. Two classification schemes have been developed, as introduced earlier for Table 1. One is according to the level of polarization with three groups, including the S group ( $|p| > \approx 70\%$ ), the M group ( $\approx 30\% < |p| < \approx 70\%$ ), and the W group ( $|p| < \approx 30\%$ ); the other is according to the variation of the polarization level and change of the sense, with three types: A, B, and C. Please, refer to earlier text in Section 2 for details.

Since at different frequencies the polarization may present different behavior during a specific event, one event can exhibit different types of polarization profiles at different frequencies. We examined all 247 event- $f$  sources and listed the result in column eight of Table 1. In Figure 10, we plotted four events with typical variation profiles, as briefly described in the following text. These profiles represent most if not all possibilities as revealed by source polarization.

- (i) Event 20120305: at all available frequencies the level does not change much with time with a fixed right-handed sense (Type A), while the level always maintains a high value above 70%. In addition, the level increases in general with frequency.
- (ii) Event 20120708: the value of  $p$  at all frequencies does not change significantly with time, while the level remains below 30%. The sense keeps to be left-handed for all frequencies, except 327 MHz at which the level is too weak to reveal the sense of polarization.
- (iii) Event 20120304: this is the reference event introduced earlier. The main characteristics are that the value of  $p$  at each frequency changes significantly with time while the sense remains to be right-handed (Type-B). For frequencies in the range of 327–445 MHz, the levels have a general declining trend from 80% to about 20%, and for frequencies in the range of 150–298 MHz, the levels present a local maximum and vary in the range of 10–70%.

**Table 4** Source numbers at available NRH frequencies, grouped according to the variation of polarization profiles. See text in Section 2, relevant to column eight in Table 1.

Frequency (MHz)	Source numbers of different groups (A, B, C)			
	A	B	C	Total
150	10	11	0	21
173	10	13	0	23
228	11	11	1	23
270	17	10	2	29
298	21	11	1	33
327	20	12	1	33
360	6	2	1	9
408	16	11	1	28
432	15	8	1	24
445	14	8	2	24
Group I	96	70	10	176
Group II	44	27	0	71
Group I+II	140	97	10	247

(iv) Event 20110307: with multiple inversions of sense at most frequencies, except the two lowest frequencies (150 and 173 MHz) at which the changes of sense are not obvious. We thus classify sources at these two frequencies to be Type-B and those at higher frequencies to be Type-C.

In the columns seven and eight of Table 1, we present the polarization characteristics of all sources. For instance, for the first event in the list (Event 20100814), the words ‘150–360 (7): B’ mean ‘for the seven frequencies in the range of 150–360 MHz the sources belong to Type-B’, and ‘408–445 (3): C’ have similar meaning, and ‘150–360 (7) (+); 408–445 (3) (I); W, M’ mean ‘the sense is right-handed for the seven frequencies in the range of 150–360 MHz, the sense is reversed for sources at the three frequencies within 408–445 MHz, and all these frequencies have weak to moderate levels of  $p$ ’.

In Table 4 we summarize the numbers of sources of Type-A, B, and C, which are 140 (57%), 97 (39%), and ten (4%), respectively. This indicates that the C type is almost negligible in number in comparison to the other two types. At the three frequencies of 150, 173, and 228 MHz, the number of Type-A sources is comparable to that of Type-B sources; at the other seven frequencies within 270–445 MHz, the number of Type-A sources is considerably larger than that of Type-B sources. The numbers of sources of Type-A, B, and C are 96 (55%), 70 (40%), and ten (6%) in group I, and 44 (62%), 27 (38%), and zero (0%) in group II. No significant difference exists between the two groups.

From Table 1 we also found that: (i) Type-A sources appear in 24 events, and more than half of the sources (at different frequencies) belong to this type in 20 events, in particular, all sources belong to this type in 12 events; (ii) Type-B sources appear in 22 events, and more than half of the sources belong to this type in 15 events, in particular, all sources belong to this type in seven events; (iii) Type-C sources appear in four events, and among them in only one event more than half of the sources belong to this type.

In Table 5, we present the total number with different values of  $p$ , and find that there exist 154, 108, and 88 sources with weak, moderate, and strong polarization, respectively. Besides, 24, 21, and 16 events contain sources with weak, moderate, and strong polarization, respectively. Sources with only weak, moderate, and strong levels of  $p$  are 86, 28, and 52,

**Table 5** Source/Event number in groups classified according to level and sense of polarization. Numbers between parentheses represent those with only that corresponding level/sense of polarization. See text in Section 2, relevant to column seven in Table 1.

	Source/Event number in groups W, M, and S			Source/Event number in groups R, L, and W			
	W	M	S	R	L	W	I
Events (Group I)	18 (7)	13 (0)	10 (3)	11 (7)	11 (4)	8 (2)	4 (0)
(Group II)	6 (1)	8 (1)	6 (2)	5 (5)	5 (5)	1 (1)	0 (0)
(Group I+II)	24 (8)	21 (1)	16(5)	16 (12)	16 (9)	9 (3)	4 (0)
Sources (Group I)	127 (74)	66 (10)	58 (35)	76	52	38	10
(Group II)	27 (12)	42 (18)	30 (17)	29	33	9	0
(Group I+II)	154 (86)	108 (28)	88 (52)	105	85	47	10

respectively. In eight, one, and five events at all available frequencies only weakly, moderately, and strongly-polarized sources exist. In group I, sources with weak polarization are the most (127), and those with moderate (66) and strong polarization (58) are comparable in number. While in group II, sources with moderate polarization are the most (42), and those with weak (27) and strong polarization (30) are comparable in number.

In Table 5, we also present the number of sources classified according to their sense. Four groups are found including sources with a single sense (left- or right-handed, referred to as L or R), sources with weak or no discernible sense (W), sources with inversion of sense (I). We find 105, 85, 47, and ten sources belonging to the four types, respectively. On the other hand, the number of events containing sources of the above four types (L, R, W, and I) are 16, 16, nine, and four, respectively. R-type sources are the most (76) in group I, while L-type sources are the most (33) in group II. In group I events containing R-type and L-type sources are both 11 in number, and in group II events containing R-type and L-type sources are both five in number.

Note that in one specific event, the characteristic of  $p$  may be different at different frequencies. For instance, for Event 20120507, in the range of 150–327 MHz sources are of R-type, and in the range of 408–445 MHz sources are of W-type; for Event 20100814, in the range of 150–360 MHz sources are of R-type, and in the range of 408–445 MHz, sources are of I-type, i.e. with inversion of sense. The number of events with only one single type of  $p$  are 12, nine, three, and zero, for types R, L, W, and I, respectively. For instance, Event 20120305 contains only the R-type sources, and Event 20140211-2 contains only L-type sources.

## 4. Summary and Discussion

Earlier statistics of IVSSs are rare and mostly based on 1D interferometric data. These studies suffered from a limited number of frequency channels, spatial and spectral resolutions, and number of events. In this study we analyze 34 events that are observed from 2010–2014 by NRH and the e-Callisto observatories. These events include 247 sources at different frequencies. For simplicity, we only analyze data with simple single-source morphology at all available frequencies during the interval of interest, and focus on characteristics such as the source spatial dispersion with frequency, the maximum brightness temperature ( $T_{\text{BM}}$ ), the  $T_{\text{BM}}$  spectra, and the degree and sense of polarization.

Major results are: (i) The majority of events (23/34) present regular and systematic source dispersion with frequency. (ii) In most (31/34) events  $T_{\text{BM}}^{\text{E}}$  is larger than  $10^8$  K and in nearly 70% (23/34) of the events it is larger than  $10^9$  K; the dominant type of  $T_{\text{BM}}$  spectra of the power-law like with a negative index, observed in 84% (21/25) of the events. (iii) In most events (30/34) the sense of polarization remains unchanged; the degree of polarization does not change significantly for a majority (140/247,  $\approx 57\%$ ) of event- $f$  sources, the degree varies significantly yet the sense remains fixed in 97 ( $\approx 39\%$ ) event- $f$  sources, and in only ten sources inversion(s) of the sense of polarization are present. These findings provide strong constraints on radiation mechanism of IVSs.

When discussing the positions of radio sources and their dispersion with frequency, effects of ionospheric and coronal refractions should be excluded to avoid spurious results (e.g. Duncan, 1981; Gary et al., 1985; Gopalswamy and Kundu, 1989b; Vasanth et al., 2016). The effect of ionospheric refraction decreases with increasing frequencies (e.g. Wild, Sheridan, and Neylan, 1959; Bougeret, 1981) and is generally small at frequencies above 150 MHz. After checking the animations of overlapped radio sources like those presented in Figure 5, positional fluctuation is observed in all cases, which might be attributed to the ionospheric refraction. However, the fluctuation is in general small and does not affect the pattern of systematic dispersion of the sources with frequency. According to Duncan (1981), coronal refraction would make radio sources look closer to the Sun, the effect might be more severe for sources with lower frequencies and limb events. At least for limb events in group I, sources at higher frequency are generally closer to the disk as shown in Figure 2a, this is inconsistent with the mentioned effect of coronal refraction. We therefore suggest that the systematic source dispersion with frequency in this study is intrinsically associated with the source properties, and not attributed to ionospheric and coronal refractions.

As mentioned in the introduction, at least two radiation mechanisms of IVSs have been proposed, which are coherent plasma emission and incoherent gyrosynchrotron. As presented in Section 3, no significant differences are found between the properties ( $T_{\text{BM}}$ ,  $T_{\text{BM}}$  spectra, and polarization) of events in group I and group II. This indicates that they may be generated by the same mechanism. Our results indicate that the majority of events present regular and systematic source dispersion, with large maximum brightness temperatures ( $> 10^8$  K in 31 events and  $> 10^9$  K in 23 events). This seems to favor coherent plasma emission which results in high brightness temperature and spatially dispersed sources with frequency. This is also supported by the conclusion that gyrosynchrotron yields emission at multi-harmonics of electron gyrofrequency, tending to result in wide-band emission from one localized source. Thus, radiation at one specific frequency may come from a large source, leading to weak or no spatial dispersion (see, e.g., Tun and Vourlidis, 2013, and Bain et al., 2014). Note that the possibility of systematic spatial dispersion of gyrosynchrotron sources due to density and magnetic field inhomogeneities cannot be ruled out completely.

We show that the IVSs present five different types of  $T_{\text{B}}$  spectral profiles. According to earlier studies (e.g. Nita, Gary, and Lee, 2004; Tun and Vourlidis, 2013; Bain et al., 2014; Morosan et al., 2019), the spectral profiles of  $T_{\text{B}}$  and flux density are also powerful means of determining emission mechanisms, and complexity of spectral profiles may be indicative of a combination of emission mechanisms. For example, Bain et al. (2014) reported a similar De-type spectrum using NRH data and attributed this to the gyrosynchrotron emission; using NRH and RSTN data Morosan et al. (2019) found spectra similar to our V-type spectra (e.g. the upper spectrum in Figure 2c) and attributed this to a combination of plasma emission and gyrosynchrotron emission. Further observational and theoretical studies are required to clarify the relationship between spectral shapes and specific emission mechanisms.

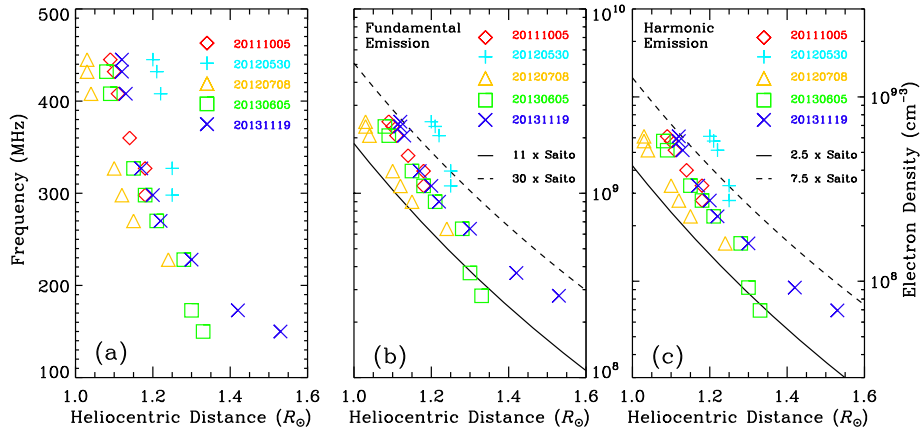


**Figure 11** (a) Averaged heliocentric distances of source centroids at available NRH frequencies for limb (L) events with significant spatial dispersion (group I), (b) radial distribution of electron density assuming fundamental plasma emission of IVSs, and (c) radial distribution of electron density assuming harmonic plasma emission of IVSs. The dotted and solid lines are given by various folds of the Saito density model.

Among the 34 events, seven limb ones are located outside the disk, and five of them belong to group I meaning that their sources are spatially dispersed with frequency. We suppose that these five events are less affected by projection than the others. Their averaged projected altitudes are shown in Figure 11a. The averaged altitudes of sources at 150, 298, and 432 MHz are in the ranges of  $1.33\text{--}1.53 R_{\odot}$ ,  $1.12\text{--}1.25 R_{\odot}$ , and  $1.03\text{--}1.21 R_{\odot}$ , respectively. Supposing IVSs are due to plasma emission at either fundamental or harmonic plasma frequency, we can infer radial profiles of coronal plasma density. In Figures 11b and c, we plot the obtained profiles under two assumptions of the emission frequency. It can be seen that for fundamental emission, plasma densities given by different events distribute within 11 and 30 folds of the Saito density model (Saito, Poland, and Munro, 1977), while for the harmonic assumption, the obtained densities distribute within 2.5 and 7.5 folds of the Saito model. Considering sources of IVSs are mostly located within or above active regions, plasmas therein are usually denser by several to ten times than those in the quiet-Sun regions or coronal holes (see, e.g., Chen and Hu, 2001, and Strachan et al., 2002). Therefore, results obtained from this figure seem to be consistent with the present knowledge on coronal densities. This also supports the suggestion that plasma emission accounts for IVSs, at least for these limb events with clear spatial dispersion.

As proposed by Vasanth et al. (2016, 2019), source properties such as plasma density and temperature can be inferred using differential emission analysis (DEM) of EUV data recorded by Atmospheric Imaging Assembly, on board the Solar Dynamics Observatory, given simultaneous data are available. The magnetic field strength can be roughly estimated using extrapolations of magnetic field on the basis of photospheric measurements. Studies along this line shall give further constraints on emission mechanisms of IVSs. In particular, the ratio of plasma frequency to electron cyclotron frequency ( $\omega_{pe}/\Omega_{ce}$ ) may be inferred, which is critical to the radiation process. If  $\omega_{pe}/\Omega_{ce} < 1$ , the mechanism could be electron cyclotron maser emission (Wu and Lee, 1979); if  $\omega_{pe}/\Omega_{ce} > 1$ , plasma emission could be the radiation mechanism. In addition, if an IVS lasts longer than the associated flare, then energetic electrons that have been injected (by the flare) and then trapped within the magnetic structures, such as post-flare loops, should be important to the radiation mechanism.

These trapped electrons may develop a loss-cone distribution and drive a kinetic electromagnetic (ECM) instability, which generates waves of upper hybrid mode, Z mode, and W mode. These modes then convert to escaping X and O modes that become the observed radio emission (see Li et al., 2019; Ni et al., 2020 for latest studies). Note that in a recent report, Carley et al. (2019) suggested that Z-mode waves excited by the loss-cone ECM instability may play a role in the origin of pulsation of a flare continuum. If an IVS occurs during the peak of the flare, then beams of energetic electrons may also play a role. It is not clear which species of energetic electrons, beamed or trapped, are decisive in the birth of IVSs.

**Acknowledgements** This study is supported by the National Natural Science Foundation of China (11790303 (11790300) and 11973031). The authors acknowledge the team of NRH for making their data available to us. We thank the Institute for Data Science FHNW Brugg/Windisch, Switzerland for providing data of the e-Callisto network.

**Disclosure of Potential Conflicts of Interest** The authors declare that they have no conflicts of interest.

**Publisher's Note** Springer Nature remains neutral with regard to jurisdictional claims in published maps and institutional affiliations.

## References

- Bain, H.M., Krucker, S., Saint-Hilaire, P., Raftery, C.L.: 2014, Radio imaging of a Type IVM radio burst on the 14th of August 2010. *Astrophys. J.* **782**, 43. DOI. ADS.
- Benz, A.O., Monstein, C., Meyer, H., Manoharan, P.K., Ramesh, R., Altyntsev, A., Lara, A., Paez, J., Cho, K.-S.: 2009, A world-wide net of solar radio spectrometers: e-CALLISTO. *Earth Moon Planets* **104**, 277. DOI. ADS.
- Boisshot, A., Denisse, J.F.: 1957, Les émissions de Type IV et l'origine des rayons cosmiques associés aux éruptions chromosphériques. *C. R. Acad. Sci. Paris* **245**, 2194.
- Bougeret, J.L.: 1981, Some effects produced by the ionosphere on radio interferometry – fluctuations in apparent source position and image distortion. *Astron. Astrophys.* **96**, 259. ADS.
- Carley, E.P., Vilmer, N., Simões, P.J.A., Ó Fearraigh, B.: 2017, Estimation of a coronal mass ejection magnetic field strength using radio observations of gyrosynchrotron radiation. *Astron. Astrophys.* **608**, A137. DOI. ADS.
- Carley, E.P., Hayes, L.A., Murray, S.A., Morosan, D.E., Shelley, W., Vilmer, N., Gallagher, P.T.: 2019, Loss-cone instability modulation due to a magnetohydrodynamic sausage mode oscillation in the solar corona. *Nat. Commun.* **10**, 2276. DOI. ADS.
- Chen, Y., Hu, Y.Q.: 2001, A two-dimensional Alfvén-wave-driven solar wind model. *Solar Phys.* **199**, 371. DOI. ADS.
- Clavelier, B., Jarry, M.F., Pick, M.: 1968, Structure of the sources of stationary Type IV b bursts and noise-storm enhancements. *Ann. Astrophys.* **31**, 523. ADS.
- Dulk, G.A.: 1973, The gyro-synchrotron radiation from moving Type IV sources in the solar corona. *Solar Phys.* **32**, 491. DOI. ADS.
- Dulk, G.A.: 1985, Radio emission from the sun and stars. *Annu. Rev. Astron. Astrophys.* **23**, 169. DOI. ADS.
- Duncan, R.A.: 1981, Langmuir-wave conversion as the explanation of moving Type-IV solar meter-wave radio outbursts. *Solar Phys.* **73**, 191. DOI. ADS.
- Gary, D.E., Dulk, G.A., House, L.L., Illing, R., Wagner, W.J., Mclean, D.J.: 1985, The Type IV burst of 1980 June 29, 0233 UT – harmonic plasma emission? *Astron. Astrophys.* **152**, 42. ADS.
- Ginzburg, V.L., Zhelezniakov, V.V.: 1958, On the possible mechanisms of sporadic solar radio emission (radiation in an isotropic plasma). *Soviet Astron.* **2**, 653. ADS.
- Gopalswamy, N., Kundu, M.R.: 1989a, A slowly moving plasmoid associated with a filament eruption. *Solar Phys.* **122**, 91. DOI. ADS.
- Gopalswamy, N., Kundu, M.R.: 1989b, Radioheliograph and white-light coronagraph studies of a coronal mass ejection event. *Solar Phys.* **122**, 145. DOI. ADS.
- Kai, K.: 1979, A statistical study of moving Type IV bursts based on Culgoora radioheliograph observations. *Solar Phys.* **61**, 187. DOI. ADS.
- Kerdraon, A., Delouis, J.-M.: 1997, In: Trotter, G. (ed.) *Coronal Physics from Radio and Space Observations, The Nançay Radioheliograph, Lec. Notes Phys.* **483**, 192. DOI. ADS.

- Li, C., Chen, Y., Kong, X., Hosseinpour, M., Wang, B.: 2019, Effect of the temperature of background plasma and the energy of energetic electrons on Z-mode excitation. *Astrophys. J.* **880**, 31. DOI. ADS.
- Liu, H., Chen, Y., Cho, K., Feng, S., Vasanth, V., Koval, A., Du, G., Wu, Z., Li, C.: 2018, A solar stationary Type IV radio burst and its radiation mechanism. *Solar Phys.* **293**, 58. DOI. ADS.
- Melrose, D.B.: 1975, Plasma emission due to isotropic fast electrons, and types I, II, and V solar radio bursts. *Solar Phys.* **43**, 211. DOI. ADS.
- Mercier, C., Subramanian, P., Chambe, G., Janardhan, P.: 2015, The structure of solar radio noise storms. *Astron. Astrophys.* **576**, A136. DOI. ADS.
- Morosan, D.E., Kilpua, E.K.J., Carley, E.P., Monstein, C.: 2019, Variable emission mechanism of a Type IV radio burst. *Astron. Astrophys.* **623**, A63. DOI. ADS.
- Ni, S., Chen, Y., Li, C., Zhang, Z., Ning, H., Kong, X., Wang, B., Hosseinpour, M.: 2020, Plasma emission induced by electron cyclotron maser instability in solar plasmas with a large ratio of plasma frequency to gyrofrequency. *Astrophys. J. Lett.* **891**, L25. DOI. ADS.
- Nita, G.M., Gary, D.E., Lee, J.: 2004, Statistical study of two years of solar flare radio spectra obtained with the Owens Valley Solar Array. *Astrophys. J.* **605**, 528. DOI. ADS.
- Pesnell, W.D., Thompson, B.J., Chamberlin, P.C.: 2012, The Solar Dynamics Observatory (SDO). *Solar Phys.* **275**, 3. DOI. ADS.
- Pick, M., Démoulin, P., Krucker, S., Malandaki, O., Maia, D.: 2005, Radio and X-ray signatures of magnetic reconnection behind an ejected flux rope. *Astrophys. J.* **625**, 1019. DOI. ADS.
- Robinson, R.D.: 1978, A study of solar flare continuum events observed at metre wavelengths. *Aust. J. Phys.* **31**, 533. DOI. ADS.
- Saito, K., Poland, A.I., Munro, R.H.: 1977, A study of the background corona near solar minimum. *Solar Phys.* **55**, 121. DOI. ADS.
- Salas-Matamoros, C., Klein, K.-L.: 2020, Polarisation and source structure of solar stationary Type IV radio bursts. *Astron. Astrophys.* **639**, A102. DOI. ADS.
- Smerd, S.F., Dulk, G.A.: 1971, In: Howard, R. (ed.) *Solar Magnetic Fields*, IAU Symposium **43**, 616. ADS.
- Stewart, R.T.: 1985, Moving Type IV Bursts In: McLean, D.J., Labrum, N.R. (eds.) *Solar radiophysics: Studies of emission from the Sun at metre wavelengths*, Cambridge Univ. Press. Cambridge. 361. ADS.
- Strachan, L., Suleiman, R., Panasyuk, A.V., Biesecker, D.A., Kohl, J.L.: 2002, Empirical densities, kinetic temperatures, and outflow velocities in the equatorial streamer belt at solar minimum. *Astrophys. J.* **571**, 1008. DOI. ADS.
- Tun, S.D., Vourlidas, A.: 2013, Derivation of the magnetic field in a coronal mass ejection core via multi-frequency radio imaging. *Astrophys. J.* **766**, 130. DOI. ADS.
- Vasanth, V., Chen, Y., Feng, S., Ma, S., Du, G., Song, H., Kong, X., Wang, B.: 2016, An eruptive hot-channel structure observed at metric wavelength as a moving Type-IV solar radio burst. *Astrophys. J. Lett.* **830**, L2. DOI. ADS.
- Vasanth, V., Chen, Y., Lv, M., Ning, H., Li, C., Feng, S., Wu, Z., Du, G.: 2019, Source imaging of a moving Type IV solar radio burst and its role in tracking coronal mass ejection from the inner to the outer corona. *Astrophys. J.* **870**, 30. DOI. ADS.
- Vlahos, L., Gergely, T.E., Papadopoulos, K.: 1982, Electron acceleration and radiation signatures in loop coronal transients. *Astrophys. J.* **258**, 812. DOI. ADS.
- Wagner, W.J., Hildner, E., House, L.L., Sawyer, C., Sheridan, K.V., Dulk, G.A.: 1981, Radio and visible light observations of matter ejected from the Sun. *Astrophys. J. Lett.* **244**, L123. DOI. ADS.
- Weiss, A.A.: 1963, The Type IV solar radio burst at metre wavelengths. *Aust. J. Phys.* **16**, 526. DOI. ADS.
- Wild, J.P., Sheridan, K.V., Neylan, A.A.: 1959, An investigation of the speed of the solar disturbances responsible for Type III radio bursts. *Aust. J. Phys.* **12**, 369. DOI. ADS.
- Winglee, R.M., Dulk, G.A.: 1986, The electron-cyclotron maser instability as a source of plasma radiation. *Astrophys. J.* **307**, 808. DOI. ADS.
- Wu, C.S., Lee, L.C.: 1979, A theory of the terrestrial kilometric radiation. *Astrophys. J.* **230**, 621. DOI. ADS.